Purdue University
Purdue e-Pubs

Birck and NCN Publications | Birck Nanotechnology Center

7-21-2014

High temperature thermoreflectance imaging and transient Harman characterization of thermoelectric energy conversion devices

T. Favaloro
University of California - Santa Cruz, Purdue University, Birck Nanotechnology Center

Amirkoushyar Ziabari
Purdue University, Birck Nanotechnology Center, aziabari@purdue.edu

Je-Hyeong Bahk
Purdue University, Birck Nanotechnology Center, jbahk@purdue.edu

P. Burke
University of California - Santa Barbara

H. Lu
University of California - Santa Barbara

See next page for additional authors

Follow this and additional works at: http://docs.lib.purdue.edu/nanopub

 Part of the Nanoscience and Nanotechnology Commons

Favaloro, T.; Ziabari, Amirkoushyar; Bahk, Je-Hyeong; Burke, P.; Lu, H.; Bowers, J.; Gossard, A.; Bian, Z.; and Shakouri, Ali, "High temperature thermoreflectance imaging and transient Harman characterization of thermoelectric energy conversion devices" (2014). *Birck and NCN Publications.* Paper 1657.
http://dx.doi.org/10.1063/1.4885198

This document has been made available through Purdue e-Pubs, a service of the Purdue University Libraries. Please contact epubs@purdue.edu for additional information.

Authors
T. Favaloro, Amirkoushyar Ziabari, Je-Hyeong Bahk, P. Burke, H. Lu, J. Bowers, A. Gossard, Z. Bian, and Ali Shakouri

This article is available at Purdue e-Pubs: http://docs.lib.purdue.edu/nanopub/1657

High temperature thermoreflectance imaging and transient Harman characterization of thermoelectric energy conversion devices

T. Favaloro, A. Ziabari, J.-H. Bahk, P. Burke, H. Lu, J. Bowers, A. Gossard, Z. Bian, and A. Shakouri

Citation: Journal of Applied Physics **116**, 034501 (2014); doi: 10.1063/1.4885198
View online: http://dx.doi.org/10.1063/1.4885198
View Table of Contents: http://scitation.aip.org/content/aip/journal/jap/116/3?ver=pdfcov
Published by the AIP Publishing

Articles you may be interested in

Thermoelectric properties of single crystal Sc1−xErxAs:InGaAs nanocomposites
J. Vac. Sci. Technol. B **31**, 041401 (2013); 10.1116/1.4810961

Direct measurement of thin-film thermoelectric figure of merit
Appl. Phys. Lett. **94**, 212508 (2009); 10.1063/1.3094880

Comparison of the 3 ω method and time-domain thermoreflectance for measurements of the cross-plane thermal conductivity of epitaxial semiconductors
J. Appl. Phys. **105**, 054303 (2009); 10.1063/1.3078808

ErAs : InGaAs/InGaAlAs superlattice thin-film power generator array
Appl. Phys. Lett. **88**, 113502 (2006); 10.1063/1.2186387

Thermoelectric power factor in semiconductors with buried epitaxial semimetallic nanoparticles
Appl. Phys. Lett. **87**, 112102 (2005); 10.1063/1.2043241

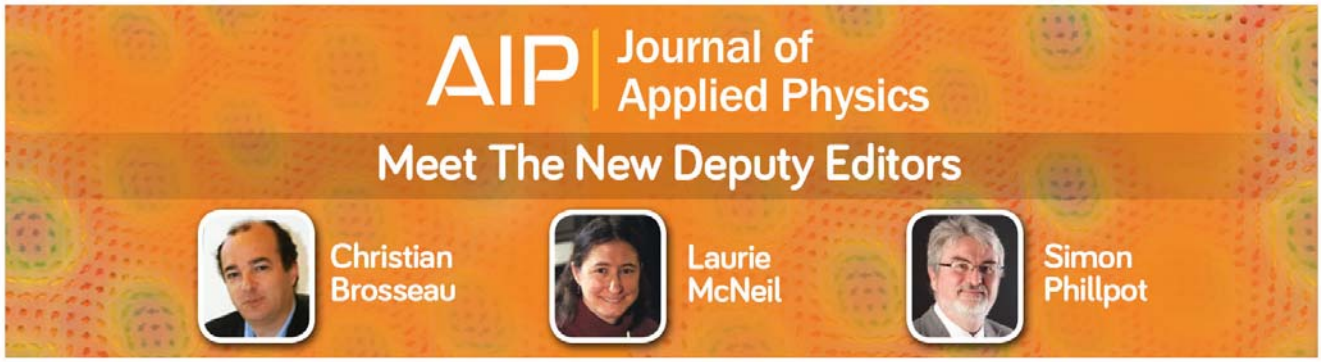

[This article is copyrighted as indicated in the article. Reuse of AIP content is subject to the terms at: http://scitation.aip.org/termsconditions. Downloaded to] IP:

JOURNAL OF APPLIED PHYSICS **116**, 034501 (2014)

High temperature thermoreflectance imaging and transient Harman characterization of thermoelectric energy conversion devices

T. Favaloro,[1,2,a)] A. Ziabari,[2,a)] J.-H. Bahk,[2] P. Burke,[3] H. Lu,[4] J. Bowers,[3] A. Gossard,[3,4] Z. Bian,[1] and A. Shakouri[1,2,b)]
[1]*Baskin School of Engineering, University of California, Santa Cruz, California 95064, USA*
[2]*Birck Nanotechnology Center, Purdue University, West Lafayette, Indiana 47907, USA*
[3]*Electrical and Computer Engineering, University of California, Santa Barbara, California 93106, USA*
[4]*Materials Department, University of California, Santa Barbara, California 93106, USA*

(Received 5 May 2014; accepted 13 June 2014; published online 15 July 2014)

Advances in thin film growth technology have enabled the selective engineering of material properties to improve the thermoelectric figure of merit and thus the efficiency of energy conversion devices. Precise characterization at the operational temperature of novel thermoelectric materials is crucial to evaluate their performance and optimize their behavior. However, measurements on thin film devices are subject to complications from the growth substrate, non-ideal contacts, and other thermal and electrical parasitic effects. In this manuscript, we determine the cross-plane thermoelectric material properties in a single measurement of a 25 μm InGaAs thin film with embedded ErAs (0.2%) nanoparticles using the bipolar transient Harman method in conjunction with thermoreflectance thermal imaging at temperatures up to 550 K. This approach eliminates discrepancies and potential device degradation from the multiple measurements necessary to obtain individual material parameters. In addition, we present a strategy for optimizing device geometry to mitigate the effect of both electrical and thermal parasitics during the measurement. Finite element method simulations are utilized to analyze non-uniform current and temperature distributions over the device area as well as the three dimensional current path for accurate extraction of material properties from the thermal images. Results are compared with independent in-plane and 3ω measurements of thermoelectric material properties for the same material composition and are found to match reasonably well; the obtained figure of merit matches within 15% at room and elevated temperatures. © *2014 AIP Publishing LLC*.
[http://dx.doi.org/10.1063/1.4885198]

I. INTRODUCTION

Thermoelectric materials have been utilized for many years as a reliable solid-state technology for applications ranging from localized hot spot cooling to waste heat recovery. Recent advances in semiconductor material synthesis leading to improved thermal-to-electrical energy conversion through material nanostructuring have made thermoelectric power generation increasingly attractive.[1–3] The maximum theoretical efficiency of a thermoelectric device is governed by a combination of material parameters, which together comprise the material figure of merit ZT, defined $ZT = \frac{S^2\sigma T}{\kappa}$. In this equation, S is the Seebeck coefficient, σ is the electrical conductivity, κ is the thermal conductivity of the material, and T is the absolute temperature. Generally, the material parameters themselves are interdependent; however, it is now possible to engineer material properties discretely on a nanoscale level by introducing complex structures and composites associated with thin-film growth. Superlattice materials and embedded nanocomposites distributed with spacing smaller than the phonon mean free path effectively scatter phonons and thus reduce thermal conductivity with minimal decrease in electrical conductivity.[4–6] Moreover, these nanostructures have been shown to decouple Seebeck and electrical conductivity through electron filtering and modification of the density of states, resulting in an enhanced Seebeck effect and improved overall ZT.[6,7]

Accurate characterization in the intended temperature range of operation is essential during the development of novel thermoelectric materials to assess and optimize their performance. Thermoelectric materials utilized for power generation are designed for specific applications that require operation in excess of room temperature. For example, average temperatures of 600 K to 900 K are typical for automobile applications[8,9] and could span from 500 K to 1300 K for deep-space missions.[10,11] Here, we utilize the transient Harman method[12,13] combined with thermoreflectance thermal imaging to determine the individual material parameters for a microscale electro-thermal energy conversion device at elevated temperatures. The transient Harman method is a simple approach to obtain the cross-plane ZT in a single measurement, and is commonly applied in the study of bulk thermoelectric materials. The individual thermoelectric parameters can be acquired with this technique if the magnitude of Peltier heating/cooling in the device is known. Little work[4,14,15] has been published applying transient measurements to thin films, which are subject to various electrical and thermal parasitic effects detrimental to the accuracy of

[a)]T. Favaloro and A. Ziabari contributed equally to this work.
[b)]Electronic mail: shakouri@purdue.edu

 © 2014 AIP Publishing LLC

[This article is copyrighted as indicated in the article. Reuse of AIP content is subject to the terms at: http://scitation.aip.org/termsconditions. Downloaded to] IP:

the method. Since these parasitic effects can dominate the overall device performance, we show how transient measurements in conjunction with thermoreflectance imaging can be used to not only extract the inherent material properties of the device but also to quantify parasitic effects. Furthermore, we discuss the design and specialized processing of experimental devices to mitigate these issues during the measurement.

II. EXPERIMENTAL METHODOLOGY

A. Transient Harman technique

The transient Harman method is a cross-plane measurement that utilizes the slower response of thermally induced voltages to distinguish between Seebeck (V_S) and resistive voltages (V_R).[12] A bipolar measurement is used to extract the Peltier (V_{SP}) and Joule (V_{SJ}) components of the Seebeck voltage since the Peltier signal flips sign with current polarity, while Joule is always heating.[13] Thus, ZT is gained in one direct measurement: $ZT = V_{SP}/V_R$.

The cross-plane ZT obtained in this manner is only accurate if the heat flux across the device is identical to the electrical current profile; specifically, all spurious electrically and thermally generated voltages are eliminated. This requires steady state and adiabatic experimental conditions. Furthermore, current must be applied uniformly across the device mesa to avoid a "distributed" Seebeck voltage effect. Finally, the average temperature of the device must not change significantly due to thermoelectric heating or cooling during the measurement.

The conventional transient Harman technique has been successfully employed for bulk material systems,[16] but these requirements are difficult to achieve for thin film devices. Both electrical and thermal paths lose uniformity at the sample surface and within the film itself due to its decreased aspect ratio. This effect is exacerbated by parasitic thermal signals; interface Joule heating as well as thermal leakage through probe leads are substantial relative to thermal signals of a film at the micrometer scale. The electrical measurement itself can also become convoluted. Parasitic electrical resistances, i.e., substrate and contact resistances, are on the order of or greater than the actual device resistance and thus a larger proportion of the measured voltage, while thermal transients are very fast and difficult to resolve above measurement noise. Analytical modeling and thermal mapping of the electrical and thermal distributions in a transient Harman experimental device have shown the detrimental impact of these parasitic effects and make more apparent the approach to minimize them.[14,15,17–19] We present an optimized design for the accurate characterization of thin films via the transient Harman technique in Sec. III A.

B. Thermoreflectance thermal imaging

In order to determine the cross-plane Seebeck coefficient and κ from the transient data, the temperature change due to the Peltier effect, ΔT_{SP}, at the device/contact interface must be known. We employed thermoreflectance imaging of the active device not only as an optical approach to quantify the surface temperature but also as a tool to visualize current uniformity and thermal leakage during the process of optimizing device geometry. Thermoreflectance thermal microscopy is a non-invasive method particularly well-suited for 2D temperature mapping of active device surfaces with submicron spatial and 10 mK temperature resolutions.[20] This optical technique is based on the detection of the change in relative reflectivity ($\Delta R/R$) of a sample due to a variance in its surface temperature (ΔT); a slight change in the temperature relative to ambient can be captured by a CCD camera as a slight alteration in reflected light. The relationship between reflectivity and sample surface temperature is expressed as $\Delta T = \frac{1}{C_{TR}}\frac{\Delta R}{R}$, where C_{TR} is the thermoreflectance coefficient—a value dependent on the sample surface material, optics used in the experimental apparatus, and illumination wavelength, among other factors. This technique is complementary for use with the transient Harman method on thermoelectric devices as they follow similar procedures for sample excitation and extraction of thermoelectric signals, and only necessitates the addition of optical (and thus non-contact) equipment in the experimental design. Additional details on CCD-based thermal imaging can be found in Refs. [21,22].

III. SAMPLE DESIGN AND FABRICATION

A. Device design optimization

Specialized processing and device lead geometries can mitigate electrical and thermal parasitic effects to improve the accuracy of the transient Harman measurement of the cross-plane ZT of novel thin film thermoelectric materials. We employed the finite element method (FEM) and analytical modeling together with thermoreflectance imaging to quantify thermal and electrical paths in thin film samples for various metallization geometries and packaging configurations.[14,18] These simulations considered 3D heat and electrical current flow throughout the device layers and included spreading in the film, heat generation, and conduction in the metal leads, as well as parasitic electrical and thermal series resistances. A schematic of an improved device design is given in Figure 1(a).

In this design, electric current is delivered to the sample mesa through a long metal lead (gold), which is electrically isolated from the thermoelectric film by a thin layer of SiO_2 (green). Electrical and thermal transport occur in the cross-plane direction through the thermoelectric material (red) to a backside electrical ground contact and thermal heat sink (gold and brown). We use separate electrodes for applied current and voltage sensing in order to reduce probe coupling and remove lead resistance from the voltage measurement. This way, the voltage sensing electrode can be connected to the device mesa with a much thinner lead to practically eliminate heat and electrical current flow to the contact, and thus ensure an open-circuit voltage measurement. Contact resistance, however, is still present in this design. Film thicknesses should ideally be maximized so that the voltage drop across the film is a relatively large fraction of the total measured voltage.

[This article is copyrighted as indicated in the article. Reuse of AIP content is subject to the terms at: http://scitation.aip.org/termsconditions. Downloaded to] IP:

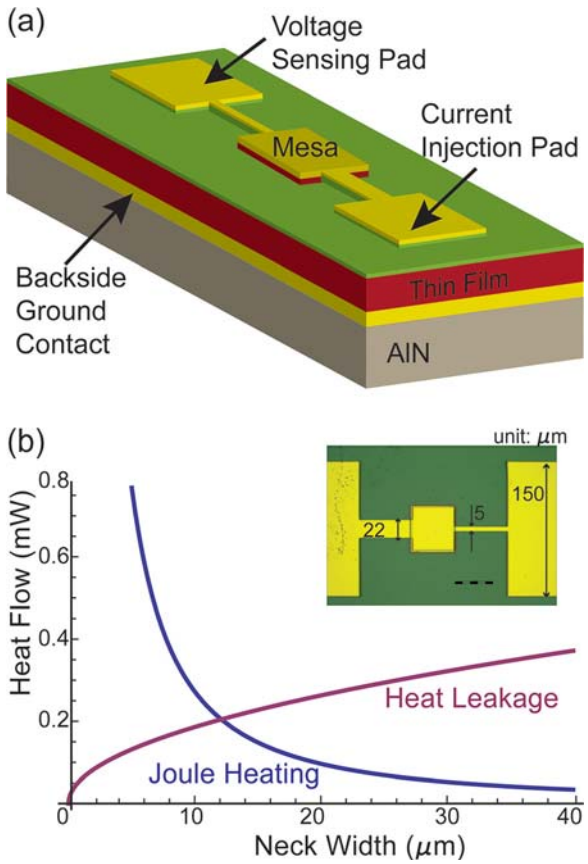

FIG. 1. (a) Schematic of improved device design for thin-film transient Harman measurement. (b) Trade-off between heat leakage through the current injection lead and heat flow into the device due to Joule heating dissipated in the lead of 25 μm thick 0.2% ErAs:InGaAs film, plotted as a function of current injection neck width. The inset shows a magnified optical image of a 50×50 μm^2 device examined in this manuscript, with a neck width of 22 μm. The thickness of the metal lead is 0.5 μm.

The use of metal leads to deliver electrical current serves to maintain thermal isolation of the device, but can exacerbate injection non-uniformity in the mesa. The magnitude of this effect is governed primarily by lead geometry and its electrical/thermal properties. A very thin lead width would minimize heat leakage via conduction into (Joule heating from probes and leads) and away from (loss of Peltier cooling) the mesa. However, Joule heating generated in the lead itself is substantially greater for a thin lead and will have greater impact. Thus, the optimized lead geometry is a trade-off between heat leakage and the influence of heat generation. Figure 1(b) plots the two effects versus current injection lead (neck) width, determined by analytical modelling as described in Wang *et al.*[23] for 25 μm 0.2%ErAs: InGaAs. The optimal neck width is calculated by minimizing the sum of these two parasitic effects; for this device, it is 21.5 μm. The inset shows a magnified optical image of the processed thin film with the mask dimensions.

The above analysis shows that these deleterious effects can be minimized, though not fully eliminated. To avoid further influence on the voltage measurement, the voltage sensing area is located on the opposite side of the sample mesa. For this manuscript, we analyzed the 25 μm thick nanostructured InGaAs film with a mesa area ranging from $50\ \mu m \times 50\ \mu m$ to $150\ \mu m \times 150\ \mu m$. Thermal images were used to assess simulation results and confirm the necessary metallization thicknesses, while determining the physical quality of the device processing.

B. Material growth and fabrication

The 25 μm thick film of n-type 0.2% ErAs: $In_{0.53}Ga_{0.47}As$ was grown via molecular beam epitaxy lattice-matched to a semi-insulating (100) InP substrate with a growth rate of 2 μm/h at a temperature of 490 °C. Si doped ($1 \times 10^{19}\ cm^{-3}$) buffer and cap layers of $In_{0.53}Ga_{0.47}As$ with 250 nm thickness were grown on the InP surface and subsequently on the film surface to minimize crystal defects in the thin film due to possible lattice mismatch. These layers also serve to improve the ohmic contact made between the film and any metallization layer for electrical contact. Erbium was co-deposited during the growth of the semiconductor matrix yielding an atomic percentage of 0.2% Er; the rock-salt structured ErAs is known to form randomly dispersed nanoinclusions of a few nanometers in diameter in InGaAs. It has been shown that incorporating ErAs nanoparticles into an InGaAs matrix significantly improves the power factor of the material through electron filtering and by donating electrons to the matrix.[6,7]

In order to eliminate any influence from the growth substrate on the measurement, we flip-chip bonded the wafer to a Au-coated AlN plate, as follows: A series of contact metals, Ni/Ge/Au/Ni/Au (Au on top) with thicknesses 5 nm, 25 nm, 35 nm, 20 nm, and 500 nm, respectively, were deposited on the thin film cap in an electron-beam evaporator. The wafer was then flip-chip bonded to a 5 μm thick Au layer previously deposited on a 400 μm thick polished AlN plate. The Au-to-Au bonding occurred at 350 °C under ~2 MPa for 2 min. The InP substrate was then removed by a wet-etch process in $HCl:H_2O = 2:1$ solution applied at room temperature for about 1.5 h, leaving the 25 μm thin film on the AlN plate with buffer layer exposed to complete the substrate transfer.

Standard photolithography procedure was used to deposit and pattern the electrodes and mesa contact. First, the same contact metal layering as described above was deposited on the substrate-transferred thin film surface. A 200 nm SrF_2 masking layer was evaporated on the contact metal to protect the metallization from the subsequent reactive ion etch of the thin film. The metals were lifted off to define the mesa areas of various sizes ranging from $50 \times 50\ \mu m^2$ to $150 \times 150\ \mu m^2$. The unmetallized thin film areas were then dry-etched away at a depth of 0.8 μm to create the device mesas using reactive ion etch with Cl_2:Ar plasma mixture under bias of 200 W. The SrF_2 masking layer was removed with deionized water after the dry etch. We then deposited a 300 nm SiO_2 insulation layer using PECVD; this layer was removed from the mesa surface by CHF_3 plasma etch to open up the mesa contact. Finally, the side contact metals of Ti/Au with thicknesses 20 nm and 500 nm, respectively, were evaporated and lifted off to pattern the side contact pads and the current/voltage electrodes.

[This article is copyrighted as indicated in the article. Reuse of AIP content is subject to the terms at: http://scitation.aip.org/termsconditions. Downloaded to] IP:

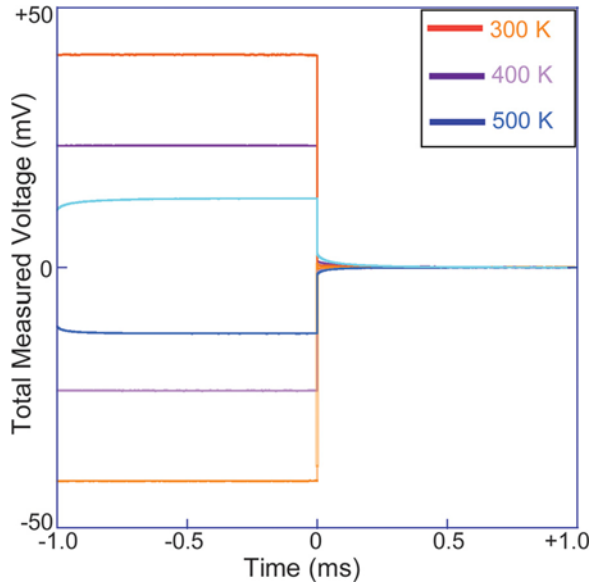

FIG. 2. The measured voltage response of the thermoelectric energy conversion device to 100 mA bipolar excitation at select ambient temperatures. The positive and negative responses are over-plotted such that time t = 0 is taken as the device turn-off time. The resistive voltage decreases with increasing temperature, while the amplitude of the transient signal is strengthened.

IV. MEASUREMENT RESULTS AND DISCUSSION

Measurements of fast thermoelectric transients and thermoreflectance imaging were performed in a high temperature thermostat with an integrated optical viewport under high vacuum ($\sim 10^{-6}$ mbar). The chamber lid is recessed to achieve the close working distance required for high magnification imaging. Sample stage and high speed circuitry, as described in Singh and Shakouri,[24] were utilized for voltage detection; with the exception that the stage used in this experiment also incorporated a high-power heater for ambient temperature control within the chamber. This configuration is capable of 100 ns temporal resolution necessary for transient detection of thinner or more thermally diffusive samples. We used a narrowband green LED ($\lambda \approx 530$ nm) for sample illumination through a microscope objective with 10× or 20× magnification and monitored the reflectivity with a Microsanj NT210B thermoreflectance imaging system. Green illumination was selected due to the relatively strong C_{TR} for Au at this wavelength.[25] We calibrated for C_{TR} in the measurement apparatus at room temperature, and determined $C_{TR} = (2.26\,6\ 0.05) \times 10^{-4}$ /K. We assumed this value for the thermal data presented in this manuscript. This was a reasonable assumption as the C_{TR} of Au is not expected to vary greatly over this temperature range and the resulting data fit well with independent measurements. Transient voltage and temperature measurements of the 0.2% ErAs:InGaAs energy conversion devices with mesa areas ranging from 50 μm × 50 μm to 150 μm × 150 μm were attained at discrete temperature steps of 50 K from room temperature up to 550 K, though the chamber has the potential to go to 1000 K.

We obtained the total voltage responses of the experimental device to bipolar square current pulsed at 500 Hz with a 50% duty cycle. The current amplitudes varied from 60 mA to 300 mA, depending on device size. The total magnitude of the measured pulse was recorded (Figure 2) in addition to a highly resolved "zoom-in" on the thermal decay for each polarity. The smallest mesa area, 50 μm × 50 μm, displayed the most uniform current/temperature distribution among the device mesa sizes examined in this experiment. In addition, it had the highest current density, and consequently, best signal to noise ratio. Therefore, the results for the 50 μm × 50 μm sized devices are presented. The measured Seebeck voltage transients for various applied currents at ambient temperature 300 K are depicted in Figure 3 for one of these of 50 μm × 50 μm devices. The insets display the extracted V_{SP} and V_{SJ} amplitudes plotted versus applied current. The Peltier

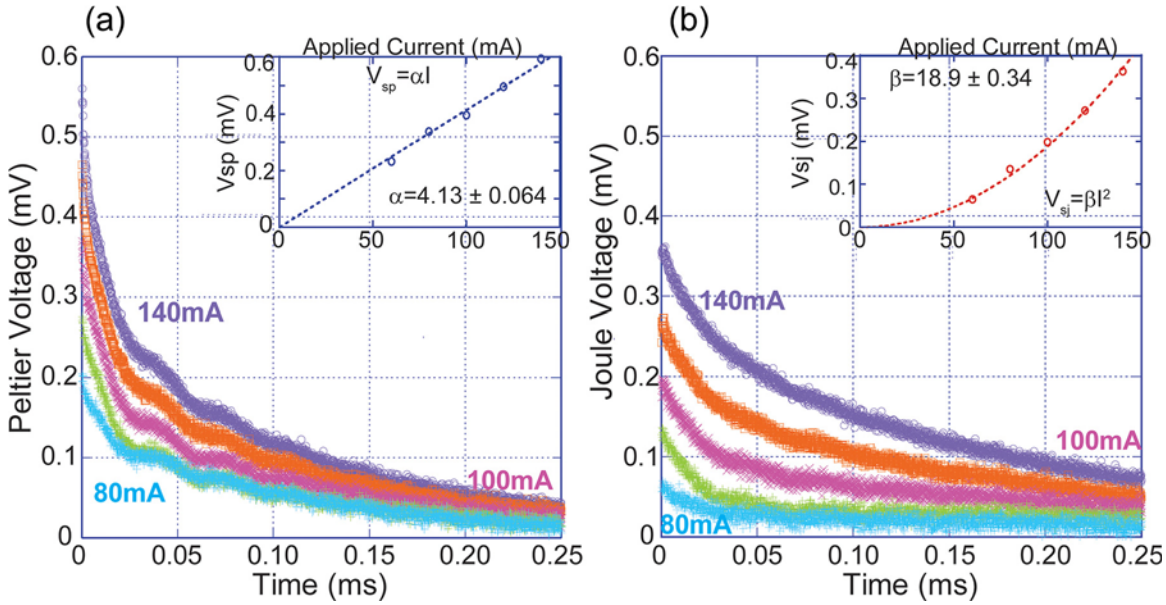

FIG. 3. The Peltier (a) and Joule (b) transient Seebeck voltages taken at various applied biases at room temperature for a 50 μm × 50 μm device. The insets display the total amplitude of the transient voltage signal plotted against input current. α and β are fitting parameters.

[This article is copyrighted as indicated in the article. Reuse of AIP content is subject to the terms at: http://scitation.aip.org/termsconditions. Downloaded to] IP:

component of the transient voltage exhibits a linear increase with current (Figure 3(a)), while the Joule component shows quadratic dependence on current (Figure 3(b)), as expected. The proper dependencies with applied bias demonstrate the accurate transient resolution of the measurement for the specific current range and temperature.

To obtain thermal images, the thermoelectric device was pulsed at the same current amplitudes as in the transient Harman measurement. An analogous procedure was used to distinguish between the Peltier (ΔT_{SP}) and Joule (ΔT_{SJ}) components of the thermal signals: Offset bipolar measurements exploited the linear and quadratic current dependencies of the Peltier and Joule temperature fields, respectively. Figure 4 shows the optical and thermal images of the same $50\,\mu m \times 50\,\mu m$ active device biased with 100 mA at 300 K, separated into Peltier and Joule components, as before. The relative phases of these surface temperature fields depict the Peltier signal as 180° out of phase with the Joule signal, indicating that the sample was cooling at this reference polarity, while Joule was always heating. The Peltier temperature distribution across the sample was uniform, varying by ~9%, due to the improved device design and the resultant current injection uniformity. The Peltier image also exhibits minimal thermal leakage into the current electrode, though some activity is still apparent in the phase image. Phase information in general is quite sensitive to small variations in the thermal distribution across the sample and thus reveals slight reflectivity changes. Joule activity for the most part is dominant in the current injection neck region, with some leakage visible into the mesa region. The uniform phase over the sample signifies the presence of Joule heating in areas where current is flowing, as expected. The magnitudes of the Peltier and Joule temperature signals are plotted versus applied bias at room temperature in Figure 4. Again, they exhibit the respective linear and quadratic dependencies.

We performed simultaneous transient electrical measurements (Figure 5) and surface temperature images (Figure 6) of the thin film device at elevated ambient temperatures, up to 550 K. The Peltier and Joule transient voltages and thermal images are presented at various ambient temperatures under a constant applied bias of 100 mA. The insets of Figure 5 show the respective Seebeck voltage signal amplitudes as a function of temperature; V_{SP} increased more rapidly than V_{SJ} with increasing temperature as anticipated by the additional temperature dependence in the V_{SP} term. A similar trend was evident when comparing ΔT_{SP} with ΔT_{SJ} over the measurement temperature range, as shown in Figure 6(b). Thus, the potential for higher energy conversion efficiency increases with temperature for this device. For brevity, Peltier and Joule thermoreflectance images at select ambient temperatures are displayed in Figure 6, along with the ΔT_{SP} and ΔT_{SJ} values averaged over the mesa plotted versus ambient temperature. Both the Peltier and Joule signals became more substantial at elevated temperatures, resulting in more significant thermal leakage in the current electrode neck. Joule heating in this region also intensified due to the increased Au resistivity with temperature. Both effects worsened temperature non-uniformity in the device,

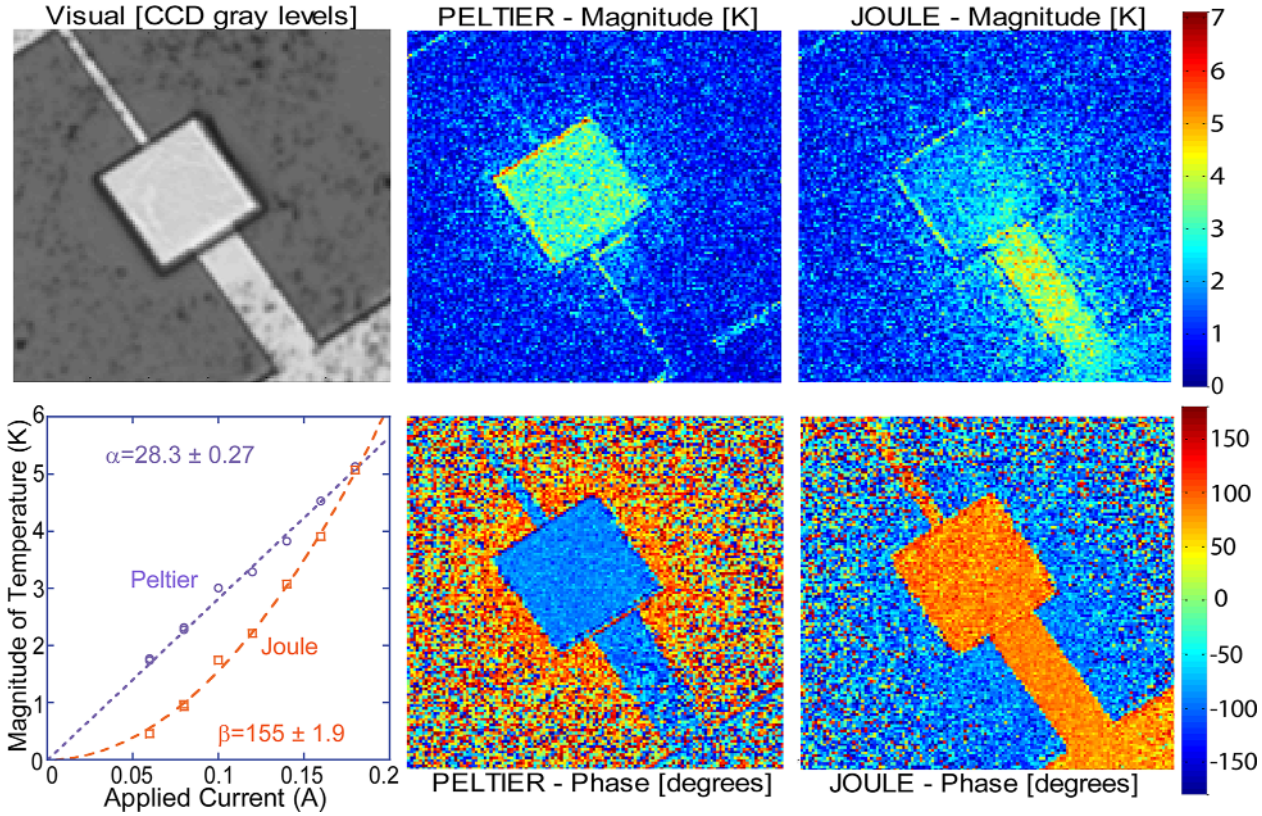

FIG. 4. Thermoreflectance imaging of the $50\,\mu m \times 50\,\mu m$ device at room temperature taken at 100 mA bias, separated into Peltier and Joule components. Color bars show the absolute temperature/phase difference from ambient. α and β are fitting parameters for the Peltier and Joule temperature amplitudes (respectively) with current.

[This article is copyrighted as indicated in the article. Reuse of AIP content is subject to the terms at: http://scitation.aip.org/termsconditions. Downloaded to] IP:

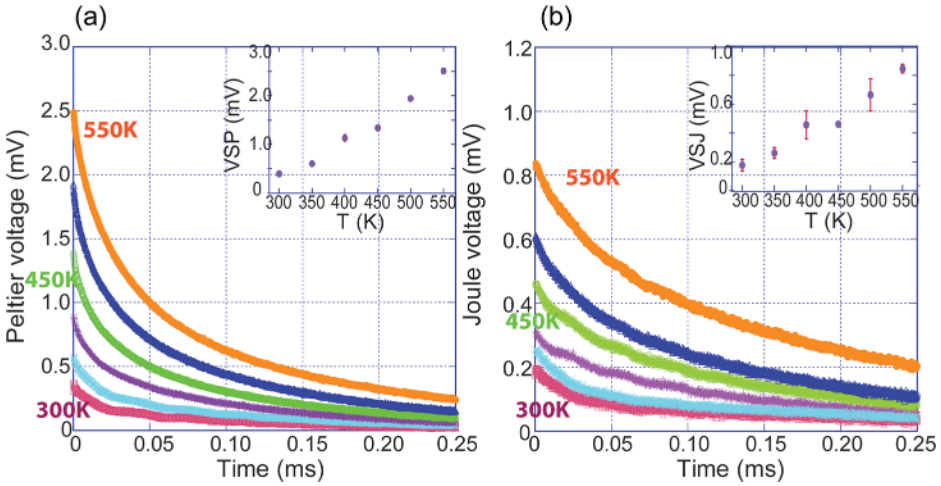

FIG. 5. Transient Seebeck voltages under ~100 mA excitation at different ambient temperatures, from room temperature to 550 K with 50 K temperature steps. (a) Peltier component of the Seebeck voltage. (b) Joule component of the Seebeck voltage. The insets show the amplitude of the respective voltage transients plotted versus ambient temperature.

which is especially apparent at ambient temperatures around 500 K and above. Moreover, the sample surface itself had an altered appearance at these temperatures. C_{TR} used in the thermal images (-2.26×10^{-4}/K) was calibrated at room temperature, and the same value was assumed at elevated temperatures in this experiment. This assumption proved to be no longer valid at or above 500 K. At these temperatures, the Au in the contact mesa unexpectedly began to diffuse into the film and slightly darkened the mesa surface, thus changing the thermoreflectance coefficient and yielding the large error bars shown in the figure.

A. Cross-plane Seebeck coefficient

Using $S = V_{SP}/DT_{SP}$, we were able to calculate the cross-plane Seebeck coefficient for the 25 μm thick 0.2% ErAs:InGaAs film, which matches very well with independent in-plane measurements. The cross-plane Seebeck coefficient is plotted in Figure 7 alongside in-plane results for a 2 μm thick 0.2% ErAs:InGaAs thin film measured using a temperature differential technique. The total error in the measurement was calculated by accounting for the dominant error sources: error in the transient voltage fitting, error in the temperature distribution across the sample as depicted in the thermal images, as well as error in the assumed value of the coefficient of thermoreflectance. Additional smaller sources of error were considered, including applied voltage fluctuations and variations in temperature readings. The large error bars at 500 K and 550 K come from the change in the appearance of the sample surface and its impact on the assumed value of C_{TR}.

V. FINITE ELEMENT MODELING

For these specially-made devices, the directly measured ZT was unexpectedly low in comparison with the ZT of 2 μm thick 0.2% ErAs:InGaAs thin film acquired from three separate in-plane (and 3ω) measurements. Since the values of the Seebeck voltages were reasonable, the main discrepancy is in the measured resistive voltages of the device,

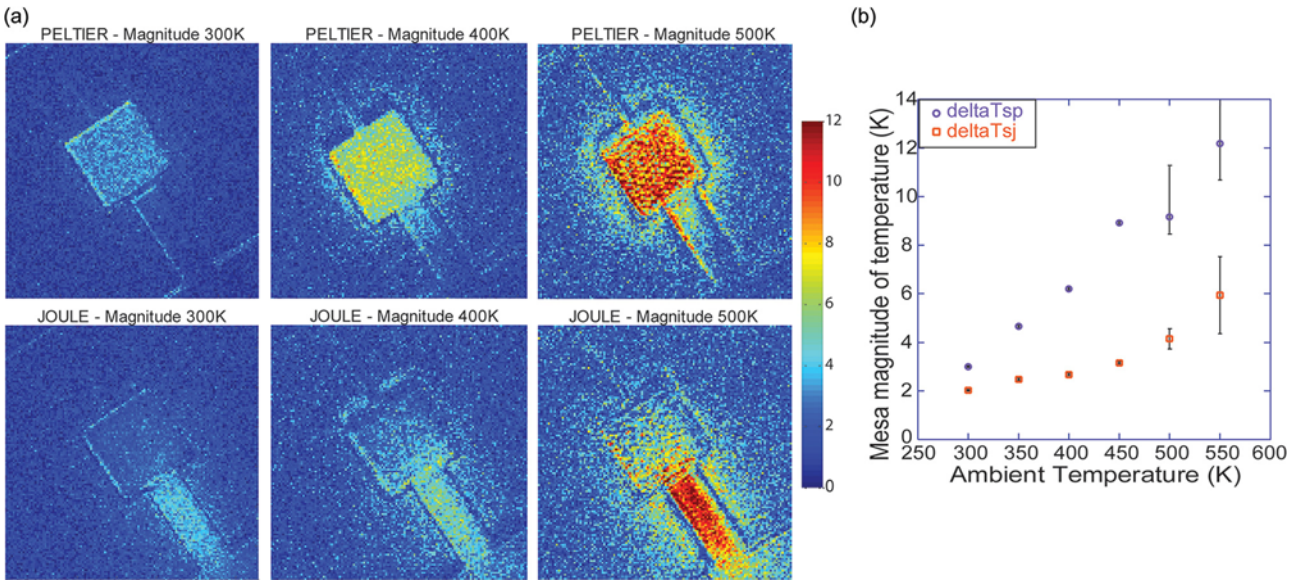

FIG. 6. (a) Peltier and Joule thermoreflectance images of the device at varying ambient temperatures: 300 K, 400 K, and 500 K. Color bar represents absolute temperature difference from ambient. (b) Peltier and Joule temperature signals averaged over the mesa plotted versus ambient temperature. The large error bars at ≥500 K are due to sample surface degradation affecting the assumed thermoreflectance coefficient of the device at the higher temperature.

[This article is copyrighted as indicated in the article. Reuse of AIP content is subject to the terms at: http://scitation.aip.org/termsconditions. Downloaded to] IP:

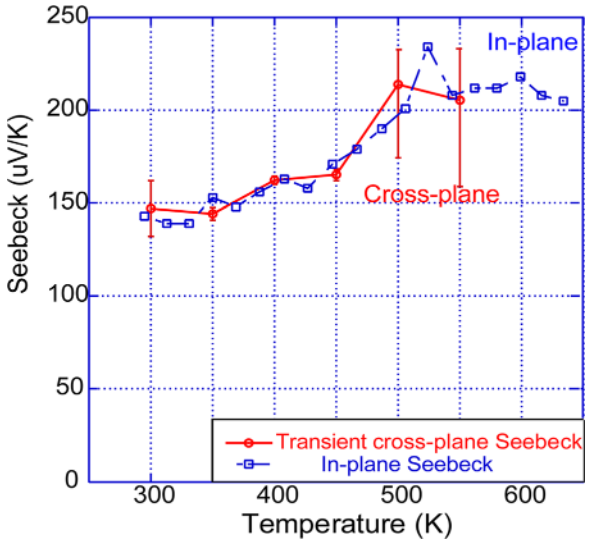

FIG. 7. Comparison of the measured Seebeck coefficient calculated in the cross-plane direction using the transient Harman technique in conjunction with thermoreflectance imaging on a 25 μm thick 0.2% ErAs:InGaAs film (red, closed circles) to that of a 2 μm thin-film measured in the in-plane direction (blue, open squares).

which were at least five times higher than anticipated and varied with the location of ground on the device. Furthermore, we observed an abnormally high degree of non-uniformity and asymmetry in the thermoreflectance images of the larger mesa areas. We employed the 3D finite element modeling software, ANSYS, to study the electrical and thermal paths to explain this aberrant behavior. From the simulation results, we found that the only scenario that reproduced the high resistive voltages and the measured thermal profiles was the removal of the backside ground contact; that is, if the current flows in the in-plane direction through the semiconductor film to a top-side grounding probe rather than the backside ground contact. This result suggests a significant interfacial contact resistance between the film and the backside ground pad likely caused by issues during processing of the devices. Both electrical resistance measurements as well as thermal images on devices of various mesa sizes were consistent with the assumption that current flows in the thin film only.

Once the electrical and thermal paths through the device were understood, we were able to extract accurate material properties of the device at room temperature. We ran the simulation iteratively for different electrical conductivity values using the measured Seebeck as input, and adjusted the

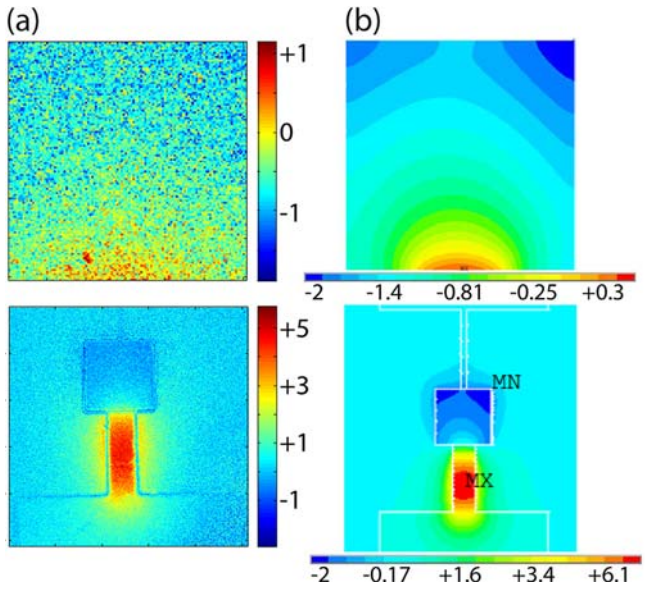

FIG. 8. Direct comparison of the measured thermoreflectance images (a) and the finite element modeling results (b) for a 50 μm $\times$ 50 μm device under 90 mA bias in cooling mode (forward bias). The top figures display a zoomed-in view of the mesa only, while the bottom set shows the device with leads. Color bars represent change in temperature (K) relative to ambient.

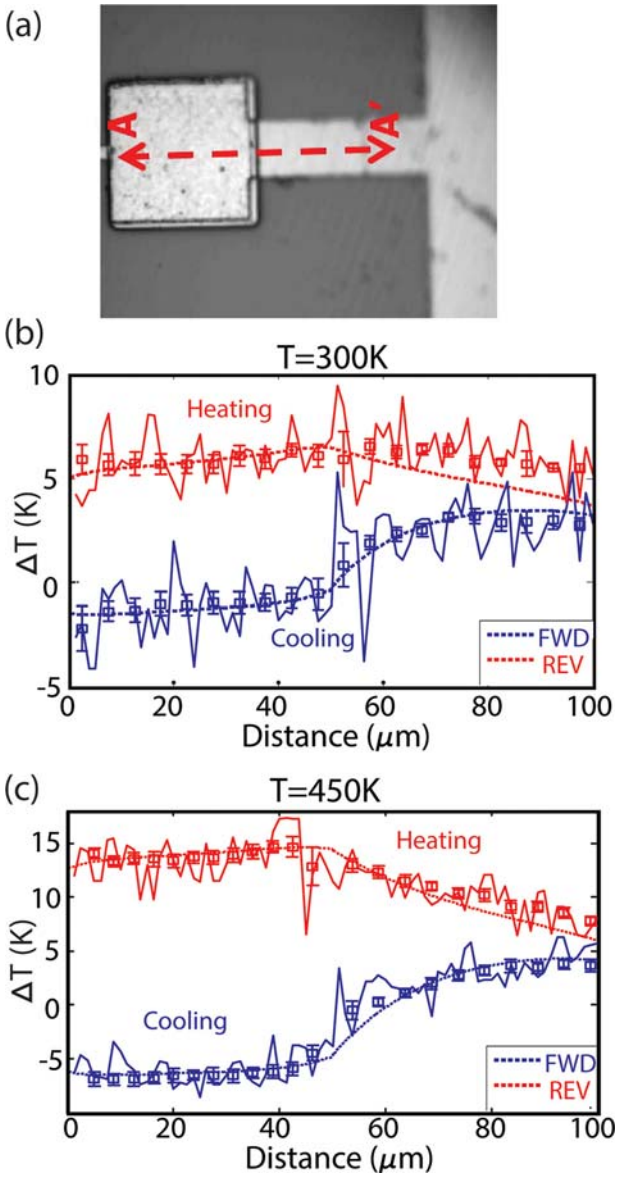

FIG. 9. Comparison of the thermal profiles between simulation (dashed lines) and thermoreflectance experiment (open squares) in forward and reverse bias (cooling and heating modes). (a) Optical image of the 50 μm $\times$ 50 μm modeled by ANSYS 3D finite element simulation. The thermal profiles displayed are the DT averaged over a box that sweeps the cross-section from A (0 μm) to A$'$ (100 μm) (squares with error bars). Solid lines are the raw data over the entire cross-section. Thermal profiles and simulation results (dashed lines) at room temperature (b) and 450 K (c).

[This article is copyrighted as indicated in the article. Reuse of AIP content is subject to the terms at: http://scitation.aip.org/termsconditions. Downloaded to] IP:

TABLE I. Summary of the 25 μm 0.2% ErAs:InGaAs material parameters in the cross-plane direction determined by either direct measurement or through FEM simulation compared alongside the reported in-plane and 3ω values of a 2 μm thin-film of the same composition.

	Seebeck coefficient (μV/K)		Electrical conductivity (X cm)$^{-1}$		Thermal conductivity (W/m K)[a]		ZT	
Data source	300 K	450 K	300 K	450 K	300 K	450 K	300 K	450 K
Independent measurement data[b]	−143	−171	872	842	4.0	2.9	0.13	0.38
Transient ZT/FEM extraction[c]	−148	−168	870	870	5.0	3.2	0.11	0.35

[a]Data from cross-plane thermal conductivity measurements on 2 μm sample using 3ω technique.
[b]Data taken on 2 μm 0.2% ErAs:InGaAs thin film.
[c]Seebeck data directly from transient ZT cross-plane measurements.

thermal conductivity of the film to achieve the best fit for the Petlier signal with the experimental results. The difference between the simulated Joule heating and the measured Joule data is used to extract the specific top contact resistivity, yielding the actual electrical resistivities of the nanostructured semiconductor material, which are 2.0×10^{-6} X cm^2 and 11.5×10^{-4} X cm, respectively. The simulated and measured thermoreflectance images in forward bias are presented side by side for a 50 μm $\times$ 50 μm device in Figure 8. In order to determine the high temperature thermal conductivity, we kept both the electrical conductivity and electrical contact resistivity constant throughout the temperature range. We expect electrical conductivity of the film to vary by ~3% over the temperature range based on in-plane van der Pauw measurements. We used the measured Seebeck values at elevated temperature as input into ANSYS and thermal conductivity was iteratively varied to achieve the best fit for both the Peltier and Joule (forward and reverse) profiles simultaneously. The simulated thermal profiles are plotted with the experimental data up to 450 K in Figure 9. The values obtained for material parameters of 0.2% ErAs:InGaAs film at 300 K and 450 K are summarized in Table I. The simulation results for different device sizes are in good agreement.

Using the correct material parameters which reflect the actual current path in the devices, we calculate the room temperature ZT of 0.114 and 0.345 at 450 K, which are, respectively, about 14 % and 8% lower than that determined by three separate measurements of the individual properties on 2 μm 0.2% ErAs:InGaAs thin film. This is primarily due to the larger thermal conductivity we determined for these devices than that measured using the 3ω technique on the 2 μm film. This may be from variations in sample growth conditions during the long-time growth of the 25 μm film. In addition, a 25 μm film may very well have different material properties than that of a 2 μm digitally grown film due to the additional contribution of long mean-free-path phonons.

VI. CONCLUSION

This work validates the use of the transient Harman technique to obtain the Seebeck voltages and thus the cross-plane ZT of thin-film energy conversion devices at high temperatures, provided an optimized device design with a good ground electrode on the substrate, as shown in Figure 1. When utilized in conjunction with thermoreflectance thermal imaging, it is a feasible approach that not only determines all cross-plane thermoelectric parameters (Seebeck coefficient and electrical and thermal conductivities) but also is a method to expose device flaws and potential failure points during a single measurement run to high temperature. We demonstrate these claims by using the collated data from the two measurement techniques on multiple device sizes: We were able to determine the nature of the device defect and simulate the three dimensional electrical and thermal paths with finite element modeling, thus successfully extracting the thermoelectric properties of the thin film.

ACKNOWLEDGMENTS

Authors would like to acknowledge Ben Curtin for assisting with the mask design. T.F., J.-H.B., Z.B., and A.S. acknowledge funding from DARPA/Army Research Office, Contract No. W911NF0810347, A.Z., P.B., H.L., J.B., A.G., and A.S. acknowledge the support from the Center for Energy Efficient Materials, an Energy Frontier Research Center funded by the U.S. Department of Energy, Office of Basic Energy Sciences under Award No. DE–SC0001009.

[1]G. J. Snyder and E. S. Toberer, Nature Mater. **7**, 105 (2008).
[2]C. J. Vineis, A. Shakouri, A. Majumdar, and M. G. Kanatzidis, Adv. Mater. **22**, 3970 (2010).
[3]A. Shakouri, Ann. Rev. Mater. Res. **41**, 399 (2011).
[4]R. Venkatasubramanian, E. Siivola, T. Colpitts, and B. O'Quinn, Nature **413**, 597 (2001).
[5]V. Rawat, Y. K. Koh, D. C. Cahill, and T. D. Sands, J. Appl. Phys. **105**, 024909 (2009).
[6]W. Kim, J. M. Zide, A. C. Gossard, D. Klenov, S. Stemmer, A. Shakouri, and A. Majumdar, Phys. Rev. Lett. **96**, 045901 (2006).
[7]J. M. Zide, J.-H. Bahk, R. Singh, M. Zebarjadi, G. Zeng, H. Lu, J. P. Feser, D. Xu, S. L. Singer, Z. X. Bian, A. Majumdar, J. E. Bowers, A. Shakouri, and A. C. Gossard, J. Appl. Phys. **108**, 123702 (2010).
[8]L. E. Bell, Science **321**, 1457 (2008).
[9]J. Yang and F. R. Stabler, J. Electron. Mater. **38**, 1245 (2009).
[10]D. T. Allen, J. C. Bass, N. B. Elsner, S. Ghamaty, and C. C. Morris, AIP Conf. Proc. **504**, 1476–1481 (2000).
[11]R. L. Cataldo and G. L. Bennett, *U. S. Space Radioisotope Power Systems and Applications: Past, Present and Future, Radioisotopes-Applications in Physical Sciences, InTech 2011* (Intech, 2011), Chap. 22.
[12]T. C. Harman, J. Appl. Phys. **29**, 1373 (1958).
[13]T. C. Harman, J. H. Cahn, and M. J. Logan, J. Appl. Phys. **30**, 1351 (1959).
[14]R. Singh, Z. Bian, A. Shakouri, G. Zeng, J.-H. Bahk, J. E. Bowers, J. M. Zide, and A. C. Gossard, Appl. Phys. Lett. **94**, 212508 (2009).
[15]Z. Bian, Y. Zhang, H. Schmidt, and A. Shakouri, in *IEEE Proceedings of 24th International Conference on Thermoelectrics, 19–23 June 2005* (IEEE, 2005), pp. 76–78.
[16]R. J. Buist, in *CRC Handbook of Thermoelectrics*, edited by R. M. Rowe (CRC, Boca Raton, 1995), Chap. 18.
[17]E. Castillo, C. Hapenciuc, and T. Borka-Tasciuc, Rev. Sci. Instrum. **81**, 044902 (2010).

[This article is copyrighted as indicated in the article. Reuse of AIP content is subject to the terms at: http://scitation.aip.org/termsconditions. Downloaded to] IP:

[18]R. McCarty, J. Thompson, J. Sharp, A. Thompson, and J. Bierschenk, J. Electron. Mater. **41**, 1274 (2012).
[19]R. Singh, Ph.D. thesis, University of California, Santa Cruz, 2008.
[20]P. M. Mayer, D. Luerssen, R. J. Ram, and J. A. Hudgings, J. Opt. Soc. Am. A **24**, 1156 (2007).
[21]M. Farzaneh, K. Maize, D. Luerssen, J. A. Summers, P. M. Mayer, P. E. Raad, K. P. Pipe, A. Shakouri, R. J. Ram, and J. A. Hudgings, J. Phys. D: Appl. Phys. **42**, 143001 (2009).
[22]S. Grauby, B. C. Forget, S. Hole, and D. Fournier, Rev. Sci. Instrum. **70**, 3603 (1999).
[23]P. Wang, A. Bar-Cohen, B. Yang, G. L. Solbrekken, and A. Shakouri, J. Appl. Phys. **100**, 014501 (2006).
[24]R. Singh and A. Shakouri, Rev. Sci. Instrum. **80**, 025101 (2009).
[25]P. L. Komarov, M. G. Burzo, and P. E. Raad, in *Proceedings of the 22nd IEEE Semiconductor Thermal Measurement and Management Symposium, Dallas, TX, 14–16 March 2006* (IEEE, 2006), pp. 199–203.

[This article is copyrighted as indicated in the article. Reuse of AIP content is subject to the terms at: http://scitation.aip.org/termsconditions. Downloaded to] IP: